PHYSICAL REVIEW C **86**, 064310 (2012)

Stabilization of prolate deformation at high spin in ^{75}Kr

T. Steinhardt, J. Eberth, S. Skoda, and O. Thelen
Institut für Kernphysik, Universität zu Köln, 50937 Köln, Germany

R. Schwengner, F. Dönau, C. Plettner,* and H. Schnare†
Institut für Strahlenphysik, Helmholtz-Zentrum Dresden-Rossendorf, 01314 Dresden, Germany

G. de Angelis and D. R. Napoli
INFN, Laboratori Nazionali di Legnaro, 35020 Legnaro, Italy

E. Farnea and A. Gadea
Instituto de Fisica Corpuscular, 46071 Valencia, Spain

A. Jungclaus
Instituto de Estructura de la Materia, Consejo Superior de Investigaciones Científicas, 28006 Madrid, Spain

K. P. Lieb
II. Physikalisches Institut, Universität Göttingen, 37073 Göttingen, Germany

R. Wadsworth
University of York, Physics Department, Heslington, York Y01 5DD, United Kingdom

(Received 1 October 2012; published 11 December 2012)

The neutron-deficient nucleus ^{75}Kr has been studied in two EUROBALL experiments. The analysis yielded a considerably extended level scheme including two newly observed excited high spin bands. The results are interpreted in the framework of the cranked Nilsson-Strutinsky approach. The calculations compare well to the experimentally established level scheme and predict the nucleus to be mainly prolate or triaxially deformed at high spin. Evidence for an oblate-prolate shape coexistence could not be found at high spin.

DOI: 10.1103/PhysRevC.86.064310 PACS number(s): 23.20.Lv, 23.20.En, 21.60.Ev, 27.50.+e

I. INTRODUCTION

The neutron-deficient nucleus ^{75}Kr belongs to the transitional mass region with $A \approx 70-80$ which includes nuclear systems ranging from weakly deformed nuclei at the shell closures at $N = Z = 28$ to the strongly deformed nuclei around ^{80}Zr [1]. The nuclear behavior is dominated generally by the low single-particle level density and in particular by the proximity of the $g_{9/2}$ orbit to the Fermi surface for both protons and neutrons. This leads to a multitude of different nuclear shapes at low spin [2–4].

This feature may ostensively be explained by the single-particle energies in the asymmetrically deformed Woods-Saxon potential as illustrated in Fig. 1. In this mass region the spherical shell gaps at $N, Z = 28, 40$, and 50 are found to lose importance. In contrast, new stabilizing energy gaps occur for $N, Z = 34, 36, 38$, and 42 at oblate and prolate shapes of various strength. Responsible for the stabilization of these deformed shell gaps are the $g_{9/2}$ and $d_{5/2}$ intruder orbits ($N = 4$). In the case of the neutron-deficient Kr isotopes the shell gaps for $N, Z = 36$ at oblate deformation, for $N = 38$ at prolate deformation, and for $N = 40$ at a spherical shape are expected to be of major importance. For ^{72}Kr, the consequence should be a favored oblate deformation, whereas in ^{73,74}Kr the prolate component should get more pronounced. In ^{75,76}Kr even influences of the spherical gap on the structure maybrk occur.

Exactly this has been experimentally discovered for the even-mass Kr isotopes. In the nucleus ^{72}Kr indications for an oblate deformation in the main component of the ground-state band at low spin have been found [6–9]. In contrast, for ^{74}Kr [6,10–12] the unperturbed oblate and prolate states are nearly degenerate, leading to strongly mixed configurations in the ground-state band. Finally, in ^{76}Kr [13,14] the influences of the oblate or spherical shell gaps are found to be very small. The result is a nearly pure prolate deformation in the ground-state band.

For the case of the odd-mass neutron-deficient Kr isotopes the first evidence for coexisting prolate and oblate shapes was found in ^{75}Kr [15,16]. The large mixing ratios deduced for the transitions connecting the low-spin yrast states were interpreted as a consequence of a mixture of oblate and prolate components. Encouraged by this unique experimental result the major aim of the present work is to investigate the development of the nuclear shapes of ^{75}Kr with rising spin.

*Present address: FLIR Radiation GmbH, 42653 Solingen, Germany.
†Present address: Globalfoundries, 01109 Dresden, Germany.

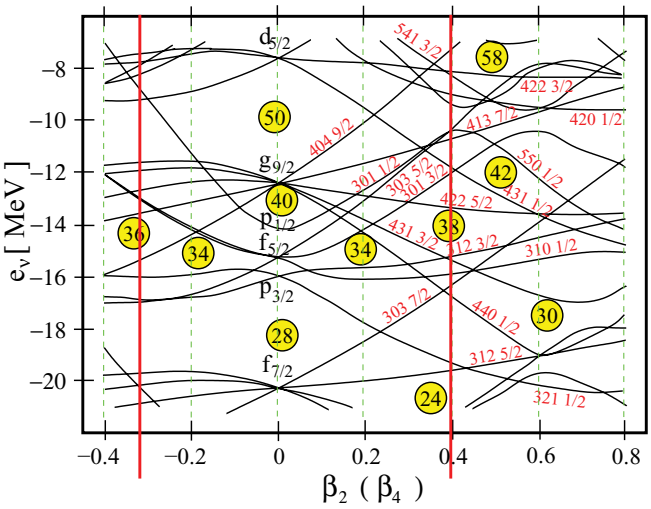

FIG. 1. (Color online) The single-particle energies in a symmetrically deformed Woods-Saxon potential as a function of the quadrupole deformation parameter β_2 [5].

II. EXPERIMENTS

Two experiments were performed at the XTU tandem accelerator of the Laboratori Nazionali di Legnaro to investigate the high-spin states of ^{75}Kr. Population of the demanded high-spin entry states in ^{75}Kr has been assured by applying the fusion-evaporation reaction ^{40}Ca(^{40}Ca,$4p1n$)^{75}Kr at beam energies of 180 MeV and 185 MeV, respectively. In the first experiment a 1 mg/cm^2 layer enriched to 99.965% in ^{40}Ca was evaporated onto a 16 mg/cm^2 gold backing, whereas the target in the second experiment consisted of a 0.9 mg/cm^2 self-supporting ^{40}Ca foil.

The evaporation codes EVAPOR [17] and CASCADE [18] predict 11.6% of the total cross section of about 1 b for the channel leading to ^{75}Kr at a beam energy of 180 MeV. This cross section of more than 100 mb indeed ensures a sufficient population of states in ^{75}Kr. On the other hand the relative cross section of less than 12% in combination with the expected entry states at angular momenta above $35\hbar$ clearly points out the need for a high granularity of the γ spectrometer and a very good reaction-channel selectivity.

The required granularity was provided by the very efficient γ spectrometer EUROBALL [19]. For a proper reaction-channel selection, additional ancillary detectors were used in the two experiments. For the identification of charged particles the Italian Silicon Sphere (ISIS) was used [20]. It consists of 40 silicon telescope detectors covering 78% of the total solid angle. Each of them consists of a 130 μm thick ΔE and a 1 mm thick E detector. The ISIS detectors were mounted inside the EUROBALL spectrometer symmetrically around the target. Furthermore, the EUROBALL section including tapered germanium detectors under forward angles with respect to the beam direction was replaced by 50 BC501A scintillation detectors in the experiment with the self-supporting target. These detectors form the Neutron Wall (NWALL) [21] providing the coincident detection of neutrons evaporated during the reaction process. In particular, these neutron detectors were essential to provide the selectivity which was extremely important for the analysis of the $4p1n$ reaction channel leading to ^{75}Kr.

The data were taken in both experiments for about 6 days. They were stored on magnetic tape under the condition that at least three germanium detectors were hit. In the second experiment an additional trigger condition demanding one neutron in coincidence to two hits of germanium detectors was used. In total, about 175 and 279 GB, respectively, of list-mode data were written to tape in the two experiments.

III. DATA ANALYSIS

The experimental data of the two experiments were analyzed with respect to two major aims. The first was to identify new excited levels by its depopulating γ transitions. The second was to assign spins by analyzing the multipole orders of the γ transitions.

All spectra of the germanium detectors were first energy-calibrated and corrected for thermal instabilities resulting from the electronics. Furthermore, the data of the composite detector systems were processed by recombining γ-ray energies deposited in neighboring crystals [22]. In the case of the experiment with the self-supporting target the Doppler shift due to the emission in flight was taken into account by another linear recalibration. Within this energy correction also the kinematical effects of the evaporated α particles onto the recoil velocity were considered. Random coincidences and delayed coincidences were suppressed by setting a prompt time window of approximately 50 ns width.

The charged-particle identification was performed by setting two-dimensional gates in the $\Delta E - \Delta E + E$ matrices corresponding to the 40 silicon telescope detectors. Hereby the mass and charge dependence of the energy deposition in the ΔE detectors has been used. The neutron-γ discrimination has been achieved by measuring the time of flight and by analyzing the shape of the detector pulse.

Optimizing the gates with respect to a minimal misidentification yielded particle identification efficiencies of 30%, 21%, and 18% for protons, α particles, and neutrons, respectively.

The nucleus ^{75}Kr was predominantly analyzed in the three-dimensional neutron-gated and non-particle-gated E_γ cubes. In the spectra mentioned below, e.g., the label (179, 254; 1115) is equivalent to a sum gate at 179 keV and 254 keV on the first and a gate at 1115 keV on the second axis of a three-dimensional symmetrical γ-energy cube.

To identify new γ-transitions and excited levels, many different particle-gated spectra were analyzed. This included symmetrical cubes up to a dimension of four. The effective detection angle for the γ rays was between 123° and 129° in the case of the experiment with the self-supporting target. This is a consequence of the combination of at least two detector types in the EUROBALL spectrometer having very different γ-ray detection efficiencies. In the calculation of the effective detection angle the symmetry of the angular distributions relative to 90° as well as the efficiencies of the individual detectors were taken into account.

To minimize systematic errors as a consequence of the high density of peaks in the spectra, two different methods for the

background subtraction were utilized [23,24]. The level order inside the bands was, in the case of levels depopulated by a single γ transition, determined by the relative intensities of the transitions. The multipole orders of the γ transitions were deduced from directional correlations from oriented states (DCO) [25,26]. The DCO analysis was carried out by exploring up to three-dimensional particle-gated and nongated spectra. In the case of three dimensions, the first gate was applied to provide a clean DCO matrix containing mainly data of the nucleus of interest. The DCO matrices were constructed by sorting the γ-ray energies registered in the cluster section against the ones detected in the clover section. The effective angles for these detector groups were 103.3° and 139.4°, respectively. In this analysis it was possible to clearly distinguish stretched $\Delta I = 2$ and $\Delta I = 1$ transitions. In contrast, for large admixtures of $\Delta I = 2$ components to the $\Delta I = 1$ transitions and for $\Delta I = 0$ transitions, the difference of the DCO ratio to stretched $\Delta I = 2$ transitions vanishes. Hence, for the unambiguous assignment of spins to the levels, two additional arguments were applied. The first results from the reaction type, in which the final nuclei are populated at very high spin. Consequently, the deexcitation via statistical and discrete depopulations to levels close to the yrast line takes also place at very high spin. Hence, the population of levels more than 1 MeV above the yrast sequence at low spin as well as decreasing or persisting spin values with rising excitation energy are unlikely. The second argument is related to the different probabilities for $E1$, $M1$, $E2$, and $M2$ transitions of a certain energy. In the case of, e.g., a level being depopulated by an $E1$ and an $M2$ transition of less than 1 MeV, the $M2$ branch should be suppressed and should have a small branching ratio.

IV. PREVIOUS RESULTS FOR ^{75}Kr

In the past two decades, many analyses of the nucleus ^{75}Kr have been performed and a comprehensive excitation scheme could be established [16,27–33]. The most complex γ-spectroscopic investigation has thereby been the one in Ref. [16]. Within this analysis, data of four different experiments were used to identify formerly unknown γ transitions and excited levels and to derive level lifetimes, spins, parities, and mixing ratios. This analysis yielded a level scheme consisting of three major bands. Their deexcitation pattern indicates the nucleus to reside in the strong coupling limit. Furthermore, some low-spin band heads and two high-spin side bands were established. The deviation of the experimental data from results of rigid triaxial-rotor-plus-particle (RTRP) calculations has, within the interpretation, been tentatively attributed to a coexistence of oblate and prolate shapes at low spin. This assumption is supported by total Routhian surface (TRS) calculations, which for low rotational frequencies predict coexisting oblate and prolate minima.

Level lifetimes of nine positive-parity states up to $I^\pi = 33/2^+$ and seven negative-parity states up to $I^\pi = 27/2^-$ were deduced using the Doppler-shift attenuation method [34] and the resulting transition quadrupole moments were compared with predictions of the projected shell model [35].

V. EXPERIMENTAL RESULTS

Positive-parity states in ^{75}Kr are shown in Fig. 2. Band 1, based on the $I^\pi = 5/2^+$ ground state [36], could be extended up to spin $I^\pi = (53/2^+)$ at an excitation energy of 16 661 keV. The in-band and interband transitions determine the level sequence up to the 9650 keV level, whereas the order of higher-lying levels is based on relative γ-ray intensities. Spins and parities are proposed according to the assignments of Ref. [16] and are supported by the derived DCO ratios listed in Table I. For the 2036 keV and the 2671 keV transitions DCO ratios could not be deduced. Hence, the spins and parities for the 11 686 and 16 661 keV levels are given tentatively. The spectra shown in Fig. 3 contain mainly peaks corresponding to transitions in band 1. At this point it has to be mentioned that in the two lowest excited states of band 1 the intensity flow shows some irregulaties for which a physical explanation cannot be given. The intensity of the 187 keV transition depopulating the $7/2^+$ state at 187 keV is 20% smaller than the sum of the intensities of the feeding transitions (584 and 191 keV) and the sum of the intensities of the transitions (378 and 191 keV) depopulating the $9/2^+$ state at 378 keV is 10% smaller than the sum of the intensities of the feeding transitions (690 and 393 keV). Neither the lifetimes nor the internal conversion may explain this deviation. Most likely, this hints to a systematic error in the determination of the intensities of the 187 and 191 keV transitions from the projection of the neutron-gated γ-ray energy matrix.

Band 5 built on the 727 keV state has been extended up to an excitation energy of 17 605 keV and a spin of $I = (57/2)$. It is connected to band 1 by four transitions (see Fig. 2). The DCO ratios of the 540, 1152, and 1513 keV linking transitions support the $I^\pi = 9/2^+$ and the $I^\pi = 13/2^+$ assignments for the 727 and the 1530 keV levels, respectively [16]. The $\Delta I = 2$ type of the 1051 and 1513 keV transitions hints to $I = 17/2$ for the 2581 keV state. Due to the regular band structure, the parities of this state and of the levels at higher excitation energy in this band are most likely positive.

The DCO ratio of the 1009 keV transition favors the assignment $I^\pi = 21/2^+$ for the 3590 keV level. The placement of the 1009 keV transition is determined by the populating 1139 keV transition.

The sequence of the in-band transitions was fixed by their relative intensities. Thereby the placement of the 1642 keV transition above the 1501 keV transition is not unambiguous, but is probable due to the development of the transition energies in the band. The spins assigned up to the 8405 keV level are supported by the DCO ratios of the in-band transitions. Above the 8405 keV state the proposed spins and parities are considered most likely due to the regularity of the band. The in-band transitions are clearly seen in the spectra (top and middle panel) in Fig. 4. The strong appearance of the 897 keV transition in the upper spectrum could hint to an unknown transition feeding band 1. This may also explain the comparably low intensity of the transitions depopulating the positive-parity yrast states above the 9906 keV level deduced in the present work.

Band 6 is connected to band 1 via the 1816, 1673, 1660, and 1877 keV transitions (see Fig. 2). The $\Delta I = 2$ character

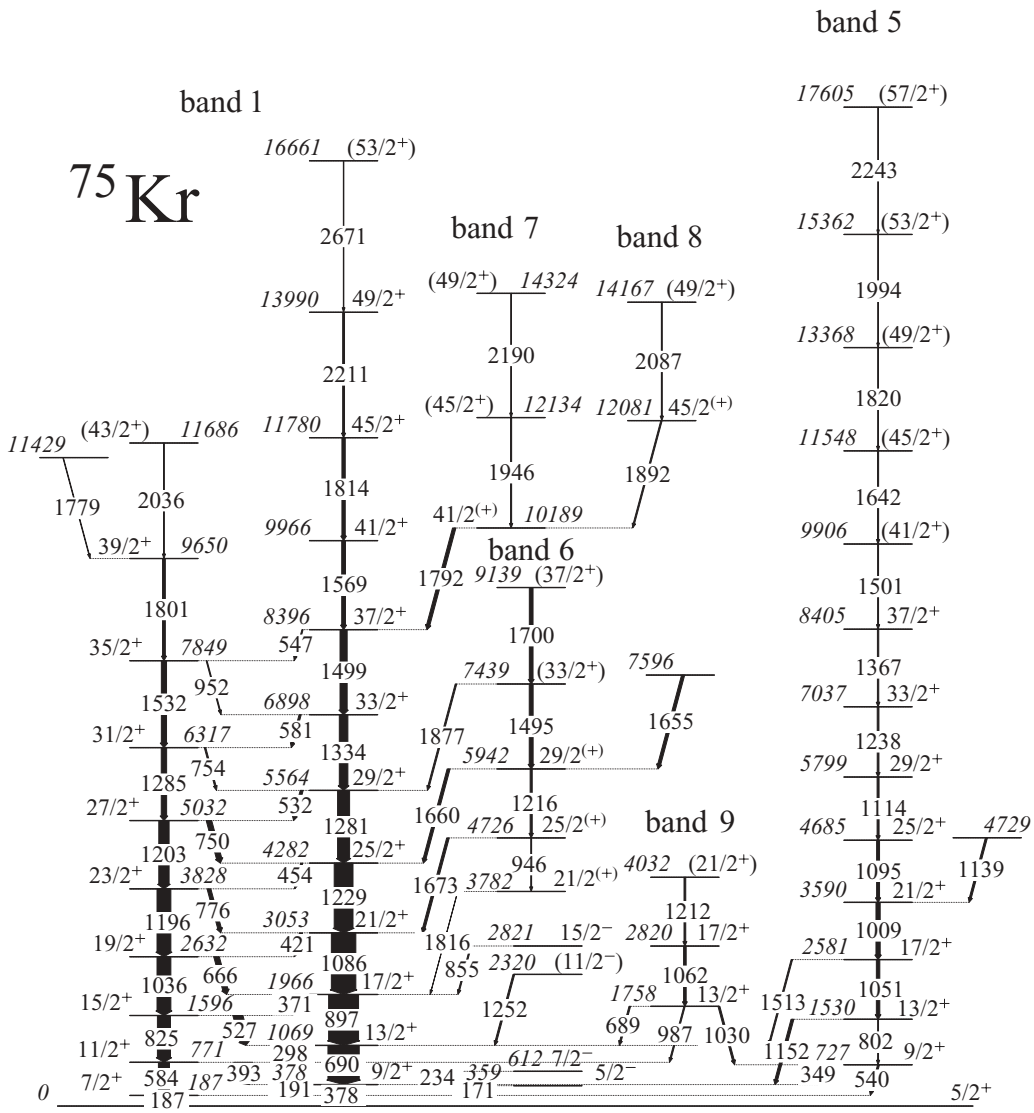

FIG. 2. Positive-parity states in ^{75}Kr and their connections to negative-parity states.

of the 1660 and 1673 keV transitions in combination with the DCO ratios of the 946 and 1216 keV in-band transitions supports the assumption of spin $I = 21/2$ for the 3782 keV level. The assigned parities are given tentatively, because a change in parity cannot be excluded from the experimental data. The spins and the parities tentatively assigned to the 7439 and 9139 keV levels are most likely with respect to the regular band structure. The bottom spectrum in Fig. 4 proves the coincidence of the 1655 and 1660 keV transitions populating and depopulating the 5942 keV level, respectively. The bands 7 and 8 feed the 8396 keV level in band 1 via the 1792 keV transition (see Ref. 2). The DCO ratios of the 1792 and 1892 keV transition support the spin and parity assignments of $I^{\pi} = 41/2^{(+)}$ and $I^{\pi} = 45/2^{(+)}$ to the 10 189 and 12 081 keV states, respectively. The parities are assigned tentatively, because a change cannot be ruled out. The upper spectrum in Fig. 5 shows the in-band transitions. The strong appearence of transitions in the negative-signature branch of band 1 is a consequence of partly gating on the 1801 keV γ ray.

The band head of band 9 is well established via the three transitions to bands 1 and 5, respectively. The spin of the 1758 keV level is limited to an upper value of 13/2 due to the 1030 keV transition to the $9/2^+$ state in band 5. The connection to the $13/2^+$ state of band 1 restricts the spin on the other hand to a lower limit of 9/2. In combination with the DCO ratios of the 987 and 1030 keV transitions and the considerations in Sec. III, the 1758 keV level has most probably $I^{\pi} = 13/2^+$. The position of the 1212 keV transition above that at 1062 keV is unambiguously given by the relative intensities. The DCO ratio of the 1062 keV transition favors spin and parity $I^{\pi} = 17/2^+$ for the 2820 keV state. In the bottom spectrum of Fig. 5 the branch populating the negative-signature state at 771 keV of band 1 is selected. The 987 keV transition is as clearly visible as the 1212 keV in-band transition.

TABLE I. Excited states and γ rays assigned to ^{75}Kr.

E_i (keV)[a]	I_i^{π} [b]	E_γ (keV)[c]	I_f^{π} [d]	$I_{\rm rel}$[e]	$I_{\rm rel}$[f]	R_{DCO}[g]	$\mathcal{R}$[h]	$\mathcal{R}$[i]
0	$5/2^+$							
179.3(2)	$3/2^-$	179.3(2)	$5/2^+$		399(77)			
187.4(2)	$7/2^+$	187.4(2)	$5/2^+$	200(10)		0.98(7)		
358.6(2)	$5/2^-$	171.3(2)	$7/2^+$	5.1(3)	2(2)		0.26(2)	0.01(1)
		179.0(1)	$3/2^-$		307(61)			0.90(24)
		358.5(3)	$5/2^+$	15(1)	31(8)	0.53(22)	0.74(6)	0.09(3)
378.4(2)	$9/2^+$	191.0(2)	$7/2^+$		193(10)	1.01(9)	0.73(5)	0.74(2)
		378.3(3)	$5/2^+$	71(4)		0.59(5)	0.27(2)	0.26(1)
612.4(2)	$7/2^-$	234.3(2)	$9/2^+$	1.4(2)	5(3)		0.006(1)	0.02(1)
		253.7(2)	$5/2^-$	181(9)	194(2)	0.96(5)	0.73(5)	0.73(3)
		433.0(3)	$3/2^-$	65(4)	71(3)	0.63(8)	0.26(2)	0.25(1)
672.5(4)		313.9(3)	$5/2^-$	1.4(3)		0.62(16)		
		493(1)	$3/2^-$					
727.4(4)	$9/2^+$	349.0(4)	$9/2^+$	10(2)			0.49(8)	
		540.1(7)	$7/2^+$	10.7(6)		1.16(16)	0.51(5)	
771.1(3)	$11/2^+$	392.8(3)	$9/2^+$	107(5)	104(4)	1.09(7)	0.62(4)	0.62(3)
		583.5(3)	$7/2^+$	65(3)	72(3)	0.35(19)	0.38(2)	0.38(2)
787.5(5)	$5/2^-$	428.7(5)	$5/2^-$		7(1)			0.21(5)
		608.4(7)	$3/2^-$		26(5)			0.79(21)
906.1(3)	$9/2^-$	293.8(2)	$7/2^-$	102(5)	94(2)	1.01(6)	0.51(3)	0.52(2)
		547.4(3)	$5/2^-$	98(6)	109(8)	0.56(8)	0.49(4)	0.48(2)
1068.8(3)	$13/2^+$	297.9(2)	$11/2^+$	74(4)	67(3)	1.01(6)	0.29(2)	0.26(2)
		690.3(4)	$9/2^+$	184(9)	191(9)	0.55(5)	0.71(5)	0.74(4)
1100.4(3)	$7/2^-$	427.9(3)		5(1)			0.24(8)	
		741.8(4)	$5/2^-$	17(4)	23(8)		0.76(25)	
1266.9(3)	$11/2^-$	360.9(2)	$9/2^-$	74(4)	66(2)	0.98(7)	0.40(3)	0.41(4)
		654.4(4)	$7/2^-$	112(6)	104(4)	0.56(4)	0.60(4)	0.58(5)
1365.0(5)	$9/2^-$	577.2(6)	$5/2^-$	19(2)	28(8)		0.43(7)	0.49(16)
		752.7(5)	$7/2^-$	24(2)[j]	22(5)	0.85(22)	0.57(7)	0.51(14)
1529.9(7)	$13/2^+$	802.2(7)	$9/2^+$	5.2(8)		0.76(46)	0.25(5)	
		1151.9(9)	$9/2^+$	16(3)	14(2)	0.60(15)	0.75(15)	
1596.0(4)	$15/2^+$	527.3(3)	$13/2^+$	57(3)	40(7)	1.1(1)	0.43(3)	0.41(4)
		824.8(4)	$11/2^+$	77(5)	67(3)	0.50(5)	0.57(5)	0.59(5)
1648.2(3)	$13/2^-$	381.4(3)	$11/2^-$	42(3)	35(3)	1.03(9)	0.29(2)	0.30(3)
		741.9(4)	$9/2^-$	102(5)	95(12)	0.55(4)	0.71(5)	0.70(6)
1757.7(6)	$13/2^+$	689.2(5)	$13/2^+$	9(1)			0.33(7)	
		987.0(7)	$11/2^+$	7.3(8)		1.33(41)	0.27(4)	
		1029.5(7)	$9/2^+$	11(3)		0.57(9)	0.40(11)	
1760.9(5)	$11/2^-$	660.5(4)	$7/2^-$	20(3)	15(6)	0.52(5)	0.61(9)	0.56(24)
		854.7(8)	$9/2^-$	13(1)	12(2)		0.39(5)	0.44(11)
1966.5(4)	$17/2^+$	370.5(2)	$15/2^+$	34(2)	24(1)	0.98(8)	0.16(1)	0.15(2)
		897.5(5)	$13/2^+$	176(11)	150(18)	0.51(4)	0.84(7)	0.85(9)
2111.4(4)	$15/2^-$	463.5(3)	$13/2^-$	35(3)	28(2)	1.02(11)	0.24(2)	0.19(3)
		844.2(4)	$11/2^-$	112(10)	107(8)	0.51(4)	0.76(9)	0.81(6)
2115.0(7)	$13/2^-$	749.7(6)	$9/2^-$	39(4)	28(2)	0.54(18)	0.57(7)	0.67(6)
		848.4(8)	$11/2^-$	30(3)	14(2)	1.05(54)	0.43(5)	0.33(4)
2320.5(8)		1251.7(7)	$13/2^+$	10(1)		0.58(6)		
2565.0(4)	$17/2^-$	453.7(3)	$15/2^-$	21(2)	14(2)	1.02(10)	0.17(2)	0.11(2)
		916.7(5)	$13/2^-$	102(6)	100(12)	0.56(5)	0.83(6)	0.89(12)
2581(1)	$17/2^+$	1050.7(7)	$13/2^+$	20(4)	14(2)	0.51(6)	0.72(15)	0.67(13)
		1513(1)	$13/2^+$	8.0(9)	7(2)	0.58(14)	0.28(5)	0.33(11)
2613.2(8)	$15/2^-$	852.3(7)	$11/2^-$	21(4)	11(2)	0.54(9)		
2632.0(5)	$19/2^+$	665.7(4)	$17/2^+$	32(2)	24(1)	1.10(9)	0.28(3)	0.27(4)
		1035.6(5)	$15/2^+$	81(6)	65(8)	0.46(4)	0.72(7)	0.73(10)
2658.1(8)	$15/2^-$	897.2(7)	$11/2^-$	12(2)				
2819.7(9)	$17/2^+$	1062.0(8)	$13/2^+$	15(2)		0.53(7)		

TABLE I. (*Continued.*)

E_i (keV)[a]	I_i^π [b]	E_γ (keV)[c]	I_f^π [d]	$I_{\rm rel}$[e]	$I_{\rm rel}$[f]	R_{DCO}[g]	$\mathcal{R}$[h]	$\mathcal{R}$[i]
2821.1(6)	$15/2^-$	500.6(7)		3.0(6)		0.83(51)	0.20(5)	
		854.9(8)[k]	$17/2^+$	7.0(9)		0.49(4)	0.46(8)	
		1554(1)	$11/2^-$	5(2)			0.35(11)	
2960.1(9)	$17/2^-$	302.7(3)	$15/2^-$	4(1)		1.27(13)	0.13(5)	
		844.5(4)	$13/2^-$	27(7)	46(8)	0.55(7)	0.87(32)	
3042.2(8)	$17/2^-$	927.2(5)	$13/2^-$	13(4)	5(4)	0.52(7)		
3052.9(5)	$21/2^+$	421.1(3)	$19/2^+$	18(2)	7(1)	1.13(19)	0.11(1)	0.06(1)
		1086.2(5)	$17/2^+$	144(9)	116(14)	0.51(3)	0.89(7)	0.94(16)
3113.8(5)	$19/2^-$	549.0(3)	$17/2^-$	20(1)	6(2)	1.06(13)	0.18(2)	0.08(2)
		1002.0(5)	$15/2^-$	91(9)	80(8)	0.51(4)	0.82(11)	0.92(12)
3345.3(6)	$19/2^-$	385.2(3)	$17/2^-$	8(1)	6(2)	1.27(10)	0.25(5)	0.44(16)
		687.5(4)	$15/2^-$	8(1)		0.47(15)	0.27(5)	
		732.7(8)	$15/2^-$	5.3(9)		0.62(6)	0.17(3)	
		1233.5(7)	$15/2^-$	9(1)	8(3)		0.30(4)	0.56(26)
3516.1(7)	$19/2^-$	473.2(6)	$17/2^-$	1.5(4)		0.86(29)	0.08(2)	
		695.5(5)	$15/2^-$	11(2)		0.54(15)	0.59(14)	
		858(1)[l]	$15/2^-$					
		902.9(7)	$15/2^-$	6(2)			0.34(11)	
3590(1)	$21/2^+$	1009.0(7)	$17/2^+$	25(5)		0.40(6)		
3627.3(6)	$21/2^-$	513.8(3)	$19/2^-$	10(1)		1.10(11)	0.12(1)	
		1061.8(5)	$17/2^-$	73(5)	60(6)	0.52(3)	0.88(7)	
(3647(1))		1033.9(8)	$15/2^-$					
3768.6(7)	$21/2^-$	423.6(3)	$19/2^-$	6(2)	6(2)	1.01(34)	0.17(7)	0.31(15)
		809.3(4)	$17/2^-$	21(5)	14(8)	0.56(6)	0.63(19)	0.69(51)
		1202.6(7)	$17/2^-$	7(1)			0.21(5)	
3782(1)	$21/2^{(+)}$	1816(1)	$17/2^+$					
3828.4(6)	$23/2^+$	775.8(4)	$21/2^+$	22(2)	13(1)	1.17(15)	0.21(2)	0.20(3)
		1196.0(6)	$19/2^+$	81(6)	55(7)	0.51(7)	0.79(8)	0.80(14)
3945.6(8)	$21/2^-$	429.8(5)	$19/2^-$	3.6(9)			0.38(12)	
		902.8(5)	$17/2^-$	6(2)		0.48(10)	0.62(21)	
4032(1)	$(21/2^+)$	1212.4(9)	$17/2^+$	10(2)				
4133.0(6)	$23/2^-$	363.5(3)	$21/2^-$	7.3(9)	3(2)	1.02(20)	0.08(1)	0.06(3)
		506.0(3)	$21/2^-$	9(1)		1.22(24)	0.11(1)	
		787.8(5)	$19/2^-$	17(2)	3(2)	0.47(10)	0.19(2)	0.06(3)
		1019.7(5)	$19/2^-$	54(5)	49(5)	0.52(7)	0.62(7)	0.89(12)
4281.9(6)	$25/2^+$	453.7(3)	$23/2^+$	11.4(9)	4(1)	0.90(12)	0.09(1)	0.05(1)
		1228.7(6)	$21/2^+$	110(8)	80(10)	0.53(3)	0.91(9)	0.95(17)
4293.5(6)	$23/2^-$	523.9(5)	$21/2^-$	3.9(6)			0.05(1)	
		667.5(4)	$21/2^-$	5.6(5)		0.91(23)	0.08(1)	
		948.5(6)	$19/2^-$	10(2)		0.47(25)	0.14(3)	
		1180.3(7)	$19/2^-$	51(5)	45(6)	0.55(7)	0.72(9)	
4432.0(7)	$23/2^-$	486.3(4)	$21/2^-$	3(1)		0.99(16)	0.16(6)	
		916(1)	$19/2^-$	16(3)		0.51(8)	0.84(23)	
4685(2)	$25/2^+$	1094.9(8)	$21/2^+$	17(6)		0.41(7)		
4726(2)	$25/2^{(+)}$	946(1)	$21/2^{(+)}$	5.2(9)		0.69(12)	0.26(5)	
		1673(1)	$21/2^+$	15(2)		0.37(8)	0.74(11)	
4729(2)		1138.6(9)		12(4)				
4741.3(6)	$25/2^-$	608.3(4)	$23/2^-$	14(1)	5(3)	1.07(18)	0.21(2)	0.27(19)
		971.7(5)	$21/2^-$	23(2)	12(3)	0.55(6)	0.35(4)	0.73(26)
		1114.6(6)	$21/2^-$	28(3)		0.54(5)	0.44(5)	
(4780(2))		1133(1)						
4821.2(8)	$25/2^-$	527.4(4)	$23/2^-$	6.5(7)			0.14(2)	
		1051.7(5)	$21/2^-$	12(1)		0.59(8)	0.26(4)	
		1195.1(6)	$21/2^-$	29(3)	29(6)	0.50(11)	0.60(8)	
4961.6(7)	$25/2^-$	529.9(3)	$23/2^-$	3.4(8)		1.54(41)	0.33(10)	
		1015.6(5)	$21/2^-$	7(1)		0.72(9)	0.67(18)	

TABLE I. (*Continued*.)

E_i (keV)[a]	I_i^{π} [b]	E_γ (keV)[c]	I_f^{π} [d]	$I_{\rm rel}$[e]	$I_{\rm rel}$[f]	R_{DCO}[g]	$\mathcal{R}$[h]	$\mathcal{R}$[i]
5031.7(6)	$27/2^+$	750.1(5)	$25/2^+$	31(3)	16(1)	0.96(15)	0.34(4)	0.35(5)
		1203.0(6)	$23/2^+$	61(7)	29(5)	0.48(5)	0.66(9)	0.65(14)
5163.0(6)	$27/2^-$	421.9(5)	$25/2^-$	6.1(9)		0.97(19)	0.09(1)	
		1029.9(5)	$23/2^-$	64(5)	52(6)	0.47(5)	0.91(10)	
5467.3(6)	$27/2^-$	646.1(5)	$25/2^-$	10(1)			0.19(3)	
		1173.8(6)	$23/2^-$	45(5)	31(8)	0.51(6)	0.81(12)	
5539.9(7)	$27/2^-$	578.1(4)	$25/2^-$	1.6(4)			0.10(3)	
		1108.2(6)	$23/2^-$	14(3)		0.56(6)	0.90(27)	
5563.7(8)	$29/2^+$	32.5(4)	$27/2^+$	17(1)	9(5)	0.78(14)	0.19(2)	0.18(10)
		1281.3(7)	$25/2^+$	71(5)	42(6)	0.55(5)	0.81(8)	0.82(18)
5799(2)	$29/2^+$	1113.8(6)	$25/2^+$	12(4)		0.39(6)		
5924.0(6)	$29/2^-$	760.9(6)	$27/2^-$	9(1)			0.19(3)	
		1182.8(6)	$25/2^-$	36(4)	18(5)	0.56(9)	0.81(11)	
5942(1)	$29/2^{(+)}$	1216.2(7)	$25/2^{(+)}$	12(2)		0.53(6)	0.42(11)	
		1660(1)	$25/2^+$	17(6)	12(2)	0.50(6)	0.58(26)	
6046.7(8)	$29/2^-$	579.7(7)	$27/2^-$	6(1)			0.17(4)	
		1225.2(7)	$25/2^-$	31(3)	17(3)	0.66(8)	0.83(12)	
6139.8(7)	$29/2^-$	600.0(7)	$27/2^-$	1.0(6)			0.15(9)	
		1178.2(7)	$25/2^-$	6(1)		0.65(14)	0.85(24)	
6317(1)	$31/2^+$	754.4(5)	$29/2^+$	8(2)	10(1)	0.88(26)	0.21(5)	0.48(7)
		1284.7(6)	$27/2^+$	32(6)	11(2)	0.56(10)	0.79(20)	0.52(11)
6359.4(6)	$31/2^-$	435.7(7)	$29/2^-$	3.2(5)			0.05(1)	
		1196.2(6)	$27/2^-$	58(5)	29(6)	0.58(10)	0.95(12)	
6688.6(7)	$31/2^-$	641.5(6)	$29/2^-$	5(1)			0.13(3)	
		1221.5(6)	$27/2^-$	33(5)	23(5)	0.63(17)	0.87(17)	
6831(1)	$31/2^-$	1290.8(7)	$27/2^-$	9(3)		0.53(8)		
6897.7(8)	$33/2^+$	580.7(3)	$31/2^+$	12(2)		0.86(23)	0.19(3)	
		1333.7(7)	$29/2^+$	50(4)	29(5)	0.50(5)	0.81(9)	
7037(2)	$33/2^+$	1238(1)	$29/2^+$	10(4)		0.42(7)		
7245.7(9)	$33/2^-$	1321.7(6)	$29/2^-$	31(3)	17(8)	0.48(11)		
7366.8(8)	$33/2^-$	678(1)	$31/2^-$	2.9(6)			0.12(3)	
		1320.0(7)	$29/2^-$	21(3)		0.55(8)	0.88(14)	
7439(2)	$(33/2^+)$	1495.1(8)	$29/2^{(+)}$	23(6)			0.73(24)	
		1877(1)	$29/2^+$	9(1)			0.27(7)	
7500(1)	$(33/2^-)$	1360(1)	$29/2^-$	5(1)				
7597(4)		1655(3)	$29/2^{(+)}$		18(7)			
7727.9(9)	$35/2^-$	1368.5(7)	$31/2^-$	45(6)	23(5)	0.54(4)		
7849.3(9)	$35/2^+$	951.7(9)	$33/2^+$	5(2)			0.15(5)	
		1531.9(7)	$31/2^+$	30(4)	9(5)	0.46(4)	0.85(17)	
8040(1)	$35/2^-$	1350.9(8)	$31/2^-$	34(5)	12(3)	0.56(4)		
8304(1)	$35/2^-$	1473(1)	$31/2^-$	7(2)		0.46(19)		
8396.4(7)	$37/2^+$	547.2(3)	$35/2^+$	7(2)		0.80(17)	0.14(5)	
		1498.6(7)	$33/2^+$	42(5)	21(3)	0.58(7)	0.86(14)	
8405(2)	$37/2^+$	1367(1)	$33/2^+$	8(3)		0.42(11)		
8699(1)	$37/2^-$	1453.7(8)	$33/2^-$	20(2)	15(3)	0.57(6)		
8842(1)	$37/2^-$	1474.7(9)	$33/2^-$	14(2)		0.65(9)		
9072(2)	$(37/2^-)$	1572(1)	$(33/2^-)$	3.5(8)				
9139(2)	$(37/2^+)$	1700(1)	$(33/2^+)$	22(5)	5(2)			
9278(1)	$39/2^-$	1549.7(7)	$35/2^-$	32(5)	11(3)	0.55(18)		
9529(1)	$39/2^-$	1489.6(8)	$35/2^-$	19(3)	8(3)	0.53(7)		
9650(1)	$39/2^+$	1801(1)	$35/2^+$	16(3)	7(2)	0.48(17)		
9906(2)	$(41/2^+)$	1501.3(9)	$37/2^+$	6(3)				
9966(1)	$41/2^+$	1569.1(8)	$37/2^+$	22(3)	9(2)	0.51(5)		
9974(2)	$(39/2^-)$	1670.0(9)	$35/2^-$	3(1)				
10189(1)	$41/2^{(+)}$	1792.3(9)	$37/2^+$	19(5)	3(2)	0.47(13)		
10283(1)	$41/2^-$	1583.7(9)	$37/2^-$	15(2)		0.63(8)		
10503(2)	$(41/2^-)$	1662(1)	$37/2^-$	8(2)	6(2)			

TABLE I. (*Continued.*)

E_i (keV)[a]	I_i^π [b]	E_γ (keV)[c]	I_f^π [d]	I_{rel}[e]	I_{rel}[f]	R_{DCO}[g]	$\mathcal{R}$[h]	$\mathcal{R}$[i]
10858(2)	$(41/2^-)$	1786(1)	$(37/2^-)$	2.2(7)				
11029(2)	$43/2^-$	1751.2(9)	$39/2^-$	22(4)		0.51(10)		
11150(2)	$43/2^-$	1621.0(8)	$39/2^-$	11(2)		0.50(13)		
11429(2)		1779(2)	$39/2^+$	3.2(7)				
11548(3)	$(45/2^+)$	1642(1)	$(41/2^+)$	6(3)				
11686(2)	$(43/2^+)$	2036(1)	$39/2^+$	5(1)				
11780(1)	$45/2^+$	1814.2(9)	$41/2^+$	19(3)		0.51(10)		
11835(2)	$(43/2^-)$	1861(1)	$(39/2^-)$	1.1(5)				
12024(2)	$45/2^-$	1740.6(9)	$41/2^-$	9(2)		0.52(9)		
12081(2)	$45/2^{(+)}$	1892(1)	$41/2^{(+)}$	8(2)		0.40(14)		
12134(2)	$(45/2^+)$	1945.6(9)	$41/2^{(+)}$	6(2)				
12381(2)	$(45/2^-)$	1878(1)	$(41/2^-)$	6(2)				
12864(3)	$(45/2^-)$	2006(2)	$(41/2^-)$	0.9(4)				
12992(3)	$47/2^-$	1843(3)	$43/2^-$	2.0(9)			0.2(1)	
		1963(1)	$43/2^-$	8(1)		0.6(2)	0.8(2)	
13019(2)	$47/2^-$	1870(1)	$43/2^-$	3(2)			0.3(2)	
		1990(1)	$43/2^-$	8(2)		0.4(3)	0.7(2)	
13368(3)	$(49/2^+)$	1820(1)	$(45/2^+)$	4(2)				
13990(2)	$49/2^+$	2211(1)	$45/2^+$	11(2)		0.41(15)		
14015(2)	$49/2^-$	1992(1)	$45/2^-$	5(1)		0.68(13)		
14167(2)	$(49/2^+)$	2087(1)	$45/2^{(+)}$	5(2)				
14324(2)	$(49/2^+)$	2190(2)	$(45/2^+)$	3.1(9)				
14407(3)	$(49/2^-)$	2026(2)	$(45/2^-)$	2.4(8)				
15020(4)	$(49/2^-)$	2156(3)	$(45/2^-)$	0.5(3)				
15218(2)	$(51/2^-)$	2199(1)	$47/2^-$	5.0(9)			0.8(2)	
		2224(4)	$47/2^-$	1.0(7)			0.2(1)	
15362(3)	$(53/2^+)$	1994(1)	$(49/2^+)$	2(1)				
16355(2)	$(53/2^-)$	2340(1)	$49/2^-$	2.1(6)				
16661(3)	$(53/2^+)$	2671(2)	$49/2^+$	2.8(6)				
17605(4)	$(57/2^+)$	2243(1)	$(53/2^+)$	1.1(7)				
17644(3)	$(55/2^-)$	2426(3)	$(51/2^-)$	3(1)				
19138(3)	$(57/2^-)$	2783(2)	$(53/2^-)$	0.8(2)				

[a]Energy of the level assigned to ^{75}Kr. The number in parentheses is the uncertainty in units of the last digit.
[b]Spin and parity of the excited state deduced from DCO ratios and deexcitation patterns.
[c]Energy of a γ transition depopulating the level at E_i.
[d]Spin and parity of the final state populated by the transition with E_γ.
[e]Relative intensity of the γ transition. The intensity of the 187 keV transition was set to 200.
[f]Relative intensity of the γ transition taken from Ref. [16]. The relative intensities were renormalized with respect to the 393 keV, 584 keV, 298 keV, and 690 keV transitions for links to positive-parity states and to the 254 keV, 433 keV, 294 keV, 547 keV, and 654 keV transitions for links to negative-parity states.
[g]vDCO ratio deduced using an $E2$ transition as the gating transition. The expected values deduced from averages of numerous known stretched $\Delta I = 1$ and $\Delta I = 2$ transitions are 0.55(2) and 1.00(3), respectively.
[h]Branching ratio.
[i]Branching ratio taken from Ref. [16].
[j]Deduced from the backed-target experiment.
[k]Incompatible DCO ratio.
[l]Energy difference of levels.

The well established band 2 is linked to band 1 through the 171, 179, 314, and 359 keV transitions (see Fig. 6). The spin and parity of the 179 keV band head were derived in previous work to be $I^\pi = 3/2^-$ [16]. Band 2 shows two regular signature branches with linking $M1/E2$ transitions in the low-energy part up to the $I^\pi = 31/2^-$ state. Above this, the sequence of the newly established transitions is fixed by the relative intensities. Spins and parities have been proposed up to the 14 015 keV level in accordance to the DCO ratios and previous analyses. The assignments for the 16 355 and 19 138 keV levels were made on the basis of the regularity of band 2. The upper spectrum in Fig. 7 shows predominantly the in-band transitions of the unfavored states in band 2 whereas in the bottom spectrum mainly the transitions between the favored states can be seen.

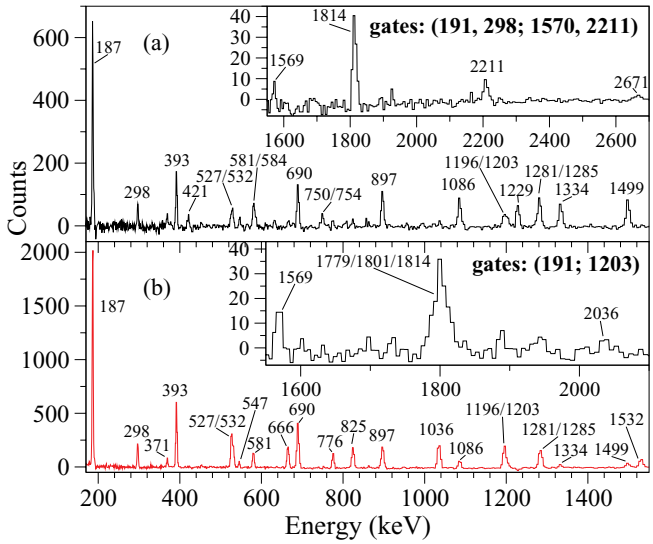

FIG. 3. (Color online) Spectra showing mainly transitions in band 1, created applying the gates to the non-particle-gated three-dimensional cube.

Band 3 shown in Fig. 6 has been well established in the low-excitation energy part in previous analyses through the intense $E2$ and $M1$ in-band transitions and the links to band 2.

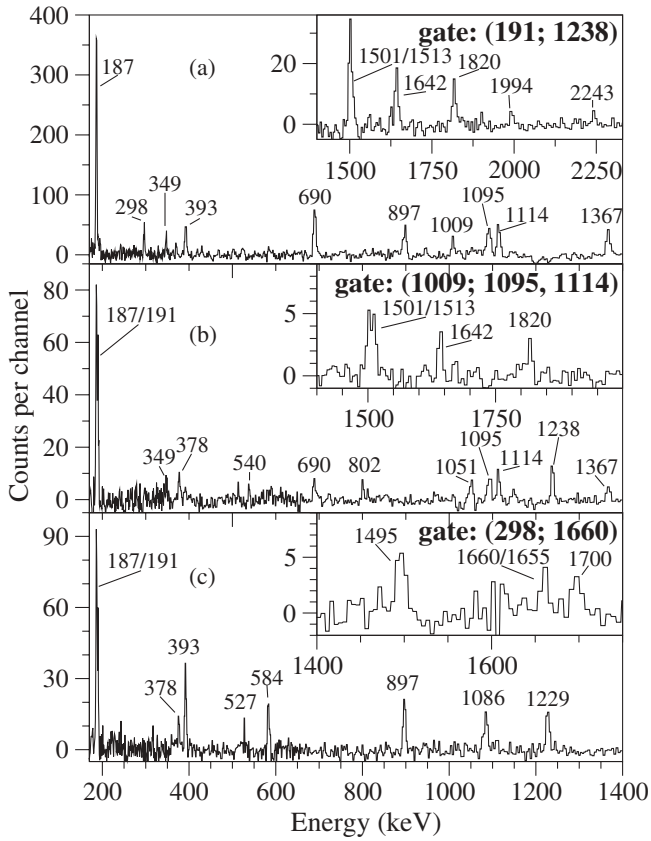

FIG. 4. Spectra created applying the gates to the non-particle-gated (top) and neutron-gated (middle) three dimensional cubes. The two topmost spectra show mainly transitions in band 5. The spectrum at the bottom shows especially the transitions depopulating the 9139 and 7439 keV levels and their connection to band 1 through the 1660 keV transition.

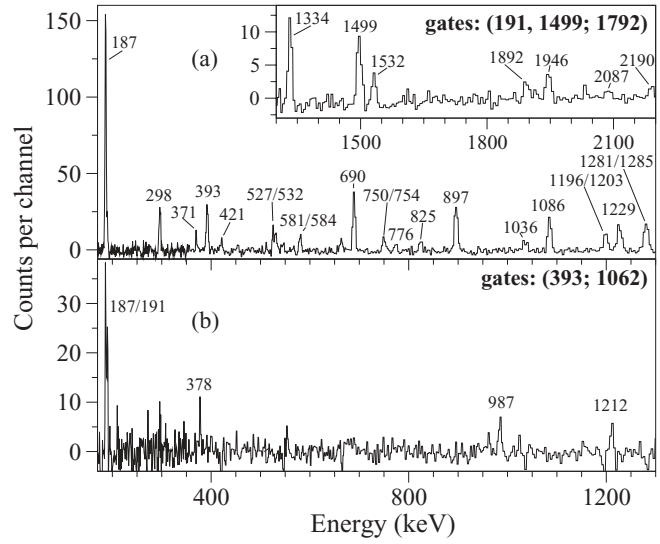

FIG. 5. Spectra obtained by setting gates in the neutron-gated three-dimensional cube. The upper spectrum contains transitions in bands 7 and 8, whereas the bottom spectrum shows the 1212 keV transition in band 9 and the connecting transition to the 771 keV level.

In this part of the level scheme, the 2658 keV level depopulating to the 1761 keV level could be added. The regular band pattern including the 303 keV and in particular the 688 keV transitions leads to spin and parity of $I^{\pi} = 15/2^{-}$ for the 2658 keV state. This is supported by the DCO ratio of the 688 keV transition indicating $\Delta I = 2$ character.

Furthermore, additional linking transitions from band 3 to bands 2 and 10 and vice versa have been identified beneath an excitation energy of 7.4 MeV. These inter-band and the in-band transitions ascertain the order of the excited states up to the 7367 keV level. Above, the relative intensities fix the sequence of the in-band transitions. Only in the cases of the 1878 and 1662 keV transitions would the inverse order also be possible. Close to 13 MeV excitation energy in the negative-signature states a band crossing with band 2 is taking place, leading to the observed interband transitions.

The spins and the parities in the low-energy part were taken from Ref. [16] in agreement with the determined DCO ratios. For higher excitation energies, the regular band pattern and the DCO ratios suggest the attributed spins and parities up to the 14407 and 17644 keV levels. For the two and three levels of highest excitation energy with negative and positive signature, respectively, the spins and parities are proposed tentatively because of the lack of DCO ratios. Figure 8 contains two spectra predominantly showing the in-band transitions between negative- (top) and positive-signature states (bottom) and the subsequent links to band 2 and band 10.

In contrast to the level scheme proposed in Ref. [16] the assignment of states of positive signature to the bands 2 and 3 above the $I^{\pi} = 21/2^{-}$ has been exchanged on the basis of systematics of the neutron-deficient odd-mass Kr isotopes ^{75,77}Kr that have very similar level schemes. As shown in Fig. 9

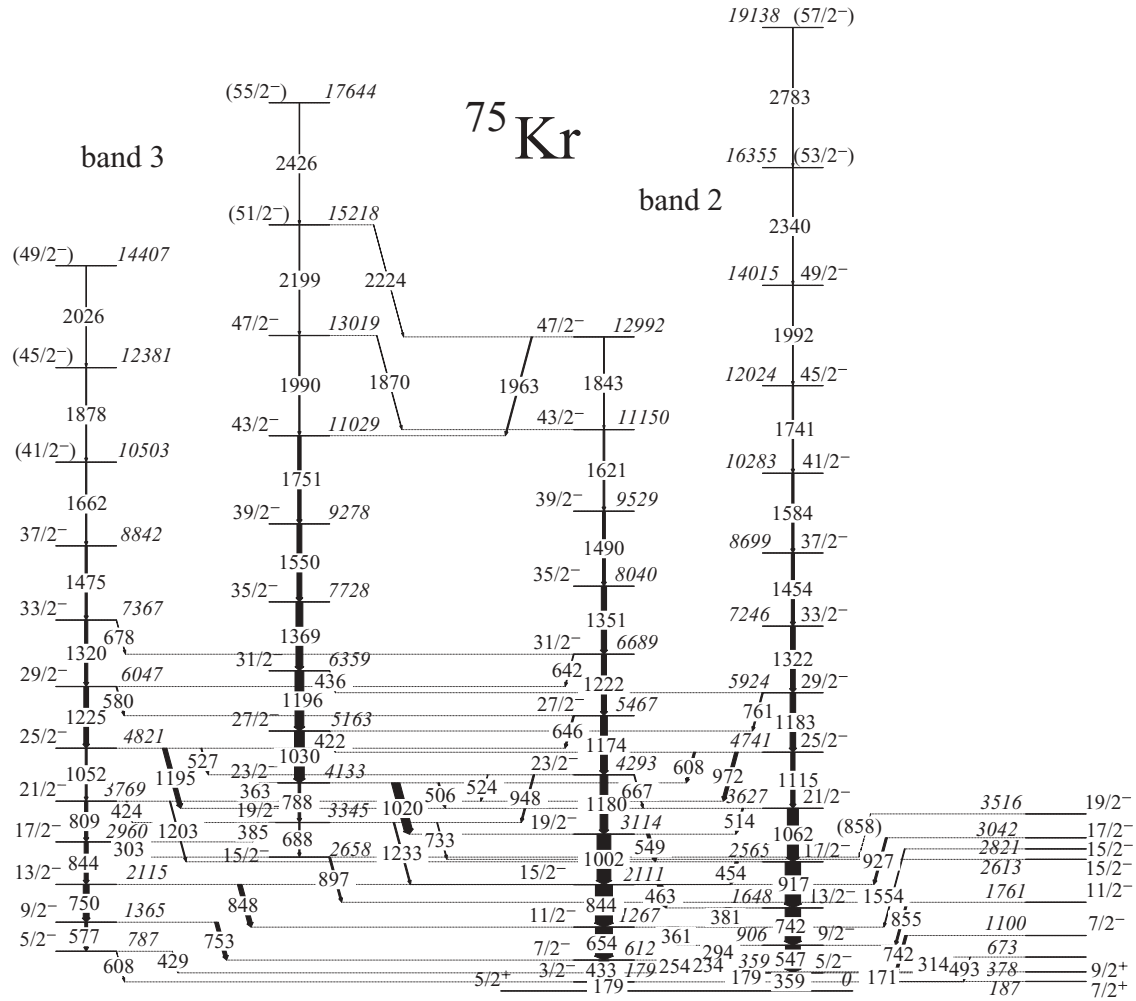

FIG. 6. The negative-parity states of bands 2 and 3. Links to other levels are shown on the left.

for band 3 in ^{75}Kr and the corresponding structure in ^{77}Kr, the signature splitting is consistent for the proposed level order, whereas the agreement of the solution published in Ref. [16] with ^{77}Kr is worse. A comparable systematic agreement has been achieved for band 2 in this way.

Band 4 has been observed in the present work for the first time. It depopulates to positive- as well as to negative-parity states as is shown in Fig. 11 and has been established up to excitation energies of 11 835 keV and 15 020 keV for negative and positive signatures, respectively. The most intense interband transition is the one at 927 keV known from previous work. It links band 4 with the 2115 keV state and its DCO ratio indicates $\Delta I = 2$ character. In combination with the general considerations in Sec. III this feature suggests an assignment of $I^{\pi} = 17/2^{-}$ for the 3042 keV level. However, the assignment is not compatible with the DCO ratio of the weak 855 keV transition depopulating the 2821 keV level. The excitation energies of the the levels in band 4 are well established through the multiple interband transitions. The $\Delta I = 1$ in-band transitions fix the sequence of the $\Delta I = 2$ transitions up to the 6140 keV level. Above that, the level order was determined on the basis of the relative intensities of the transitions. For the deexcitation of the levels above the 8304 and 6140 keV levels of negative and positive signature, respectively, a DCO analysis could not be performed. The top and middle spectra in Fig. 10 contain mainly the in-band transitions of band 4 between states of negative and positive signature. These spectra demonstrate the weak population of this band in comparison with the excited levels in the proximity of the yrast states.

In the already known band 10, an excited level at 673 keV state populating band 2 has been established (see Fig. 11). The DCO ratio of the 314 keV transition favors spin and parity $I^{\pi} = 5/2^{-}$ or $I^{\pi} = 9/2^{-}$ for the 673 keV state. This does not fit well with the higher-lying $\Delta I = 2$ sequence and has therefore not been marked in the level scheme. Additionally, two deexcitations of higher-lying levels in this band have been identified. The sequence could not unambiguously be determined from the spectra because the transition energy of 1034 keV is close to the intense 1030 keV γ ray. This may be seen in the bottom spectrum of Fig. 10. The peak at approximately 1030 keV, which is remarkably large compared with the peaks at 688, 788, and 897 keV, is considered as the superposition of the 1030 and 1034 keV γ rays.

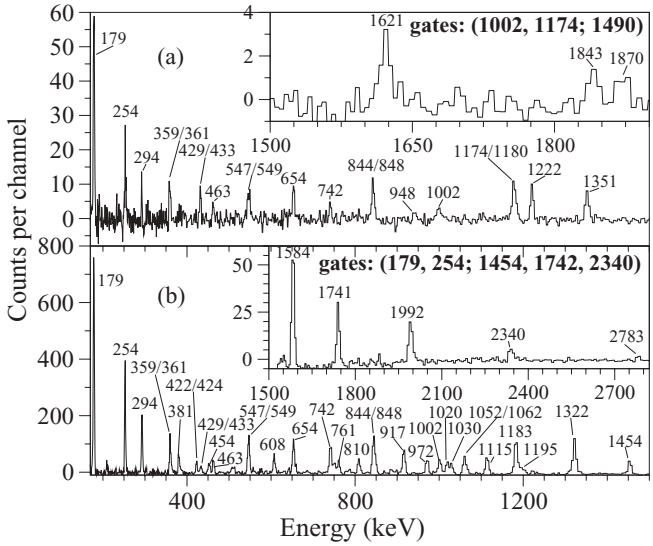

FIG. 7. These spectra are obtained by setting the gates in the neutron-gated three-dimensional cube. The spectra contain in the high-energy part mainly the lines corresponding to decays in band 2 in between negative- (top) and positive-signature states (bottom).

Summarizing the experimental results discussed above, the level scheme of ^{75}Kr has been considerably extended in the present analysis. This extension includes newly established bands as well as the extension of known sequences and the rejection of levels proposed earlier. All the extracted experimental data are listed in Table I. For comparison, the branching ratios and the relative intensities deduced in Ref. [16] are also given. The tendency toward lower intensities

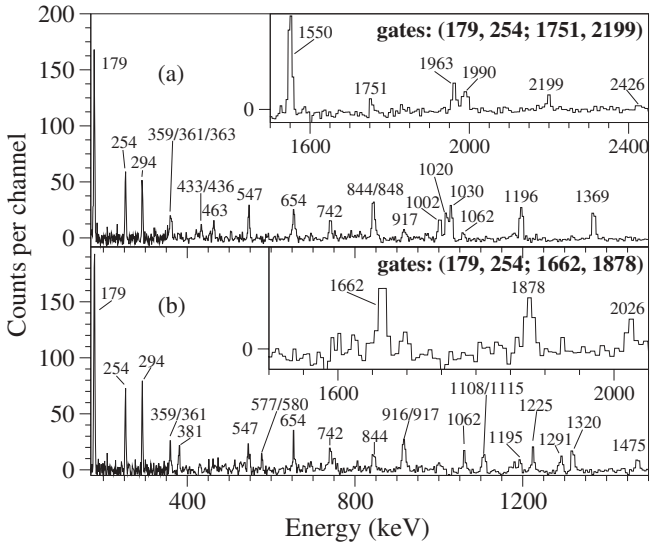

FIG. 8. Spectra created by setting gates in the neutron-gated three-dimensional cube. The top spectrum contains in the high-energy part only peaks corresponding to transitions between negative-signature states of band 3. In the bottom spectrum, mainly showing transitions in the positive-signature branch of band 3, contaminants in the gates lead also to the occurrence of peaks belonging to transitions in band 4.

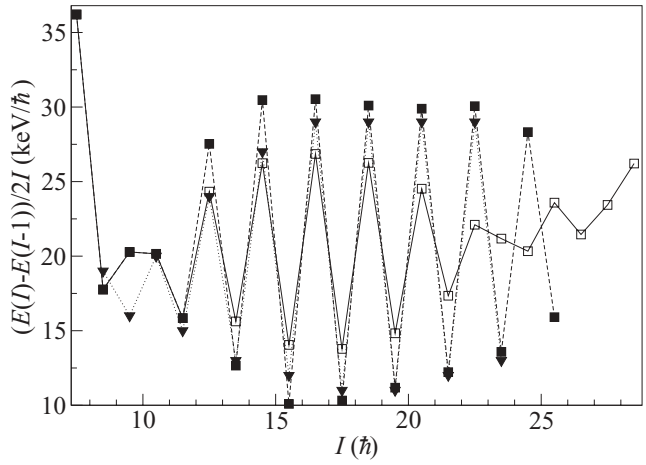

FIG. 9. The signature splitting in band 3 for the nucleus ^{75}Kr (squares) is very similar to that in ^{77}Kr (triangles). The open squares label the splitting based on the level assignments to band 3 given in Ref. [16].

at high spins in the data of Ref. [16] compared with the present ones thereby reflects the higher-lying entry region in the present experiment.

VI. CNS CALCULATIONS FOR ^{75}Kr

The structure of ^{75}Kr containing various high-spin bands has been interpreted in the framework of the configuration-dependent cranked Nilsson-Strutinsky approach [37]. This model was chosen because it has proven a good capability of describing collective high-spin excitations all over the nuclide chart. It is based on the cranking model, and the single-particle energies are adjusted to nuclei of the $A \approx 80$ mass region. It predicts an excitation energy minimized with respect to the deformation parameters ϵ_2, ϵ_4, and γ for a certain spin and a given configuration. In this way, the model allows the assignment of deformations to the high-spin states through the identification of the configuration providing the best agreement between calculated and experimental excitation energies for the different excited states of a band. As in the cranking model, signature and parity are good quantum numbers in this approximation.

Pairing correlations, which empirically are considered to play a minor role at high spin, are neglected as well as the mixing of different configurations. According to these assumptions, the predictions of the calculations are compared with the experimental results for levels with spins $I > 10\hbar$ only. The configurations are given by fixing the number of particles in the orbits of the highest spin and in all the others for each oscillator shell, separately for protons and neutrons and the different signatures $\alpha = \pm 1/2$. Because the Fermi level of protons and neutrons for the nucleus ^{75}Kr is close to the $N = 4g_{9/2}$ orbit, excitations to the $h_{11/2}$ intruder orbit can be neglected.

The configurations are in the following labeled by their number of protons and neutrons in the $N = 4g_{9/2}$ shell, $(p_{N=4,g_{9/2}}, n_{N=4,g_{9/2}})$. The parity and signature of each band

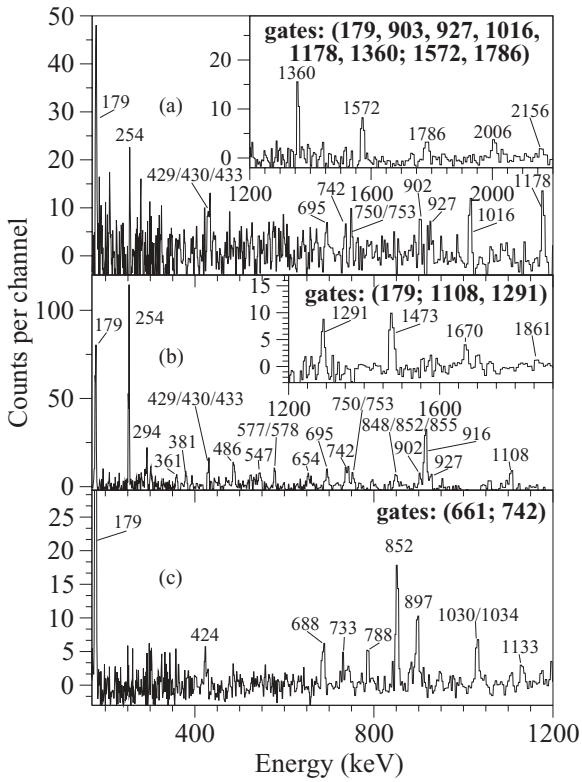

FIG. 10. Spectra demonstrating the weak population of the positive- (top) and negative-signature states (middle) of band 4. They were obtained by setting gates in the neutron-gated three dimensional cube. In the top spectrum, the in-band and tentatively unobserved interband transitions reduce the intensity of the $\Delta I = 2$ transitions. The bottom spectrum clearly shows the 852 and 1034 keV in-band transitions in band 10 as well as the 733 and 897 keV γ rays out of band 3.

is given explicitly in each chapter and in the figure captions. Configurations with the same number of protons and neutrons in the $g_{9/2}$ shell, but different occupation of the fp shell, are labeled as $(p_{N=4,g_{9/2}}, n_{N=4,g_{9/2}})-1$, $(p_{N=4,g_{9/2}}, n_{N=4,g_{9/2}})-2, \ldots$.

Band 1 in ^{75}Kr is built on the $I_\pi = 5/2^+$ ground state. The $E2/M1$ deexcitation pattern in combination with the small signature splitting suggests that the nucleus is in the strong coupling limit. Referring to the single-particle energies in a deformed potential (see Fig. 1), the only possible explanation is that the unpaired neutron occupies the [422]5/2 orbit at a prolate deformation of about $\epsilon_2 = 0.4$ or an oblate one of approximately $\epsilon_2 = 0.35$. Consequently, there are five neutrons and at least two protons expected to occupy the $g_{9/2}$ orbits. In agreement to these considerations the best reproduction of the experimental data is achieved through a (2,5) configuration for both, positive- and negative-signature states (see Fig. 12). Although the absolute excitation energy is overestimated in the calculations, the development of the energies with rising spin is very well described. The nuclear shape resides for the whole band above spin $I = 10$ close to collective prolate. Merely a slight trend to less collective triaxiality associated with a drop of the deformation parameter value from $\epsilon_2 \approx 0.33$ to $\epsilon_2 \approx 0.23$ can be noticed with rising spin (see Fig. 13).

In band 5, only positive-signature states have been observed, although the levels lie close to or form the yrast states of positive parity. Hence, the negative-signature states seem to be highly unfavored. Under the assumption of axial symmetry this hints to strong Coriolis effects. Referring to the single-particle energies in the deformed potential (see Fig. 1) and restricting to one-quasiparticle (1qp) excitations, the [440]1/2 orbit would be the only candidate explaining the $I_\pi = 9/2^+$ band head and the strong signature splitting. This should result for both particle and hole excitations at a moderate prolate deformation. On the other hand, the energy of the $13/2^+$ to $9/2^+$ transition indicates a large deformation. Assuming the nucleus to be in the decoupling limit and applying the Grodzins rule [38], this decay energy is equivalent to a quadrupole deformation of $\epsilon_2 > 0.3$. Furthermore, the TRS calculations in Ref. [16] predict an oblate minimum at $|\beta_2| > 0.3$ which also contradicts the configuration in which the unpaired neutron occupies the [404]9/2 orbit. In conclusion, the most probable solution, which would agree with the TRS calculations, is the oblate deformed configuration with two protons and five neutrons in the $g_{9/2}$ orbit and the unpaired neutron occupying the [422]5/2 orbit. The band head with $I^\pi = 5/2^+$ as well as the negative-signature states may not yet have been observed due to the depopulation via the strong interband transitions close to the band head. Furthermore, such an oblate deformed configuration is not expected to persist up to high spin, but should be crossed by a prolate or triaxial band.

This thesis is compliant with the CNS calculations, which favor an assignment of a configuration with three protons and four neutrons in the $g_{9/2}$ orbit at high spin [labeled "(3,4)-1" in Fig. 12]. This is equivalent to an at least three-quasiparticle (3qp) excitation consisting of the unpaired neutron and a broken fp-shell proton pair. The development of the experimental excitation energies as a function of the spin is well described. The shift up in energy with respect to the (2,5) configurations has two different reasons. On the one hand, it is a consequence of the overestimated single-particle energies for the $g_{9/2}$ orbit, yielding systematically lower excitation energies for configurations with just two protons in the $g_{9/2}$ orbit. On the other hand, a mixing due to the close-lying (3,4)-1 and (3,4)-2 configurations could in this case be responsible for another reduction of the experimental excitation energies in band 5. The deformation in band 5 starts at $\epsilon_2 = 0.34$ and $\gamma = -18^\circ$ for the $I = 21/2$ state and above $I = 55/2$ it is smoothly changing to a noncollective oblate deformation. At a spin of $I = 65/2$, this configuration is predicted to terminate at a spin of $I = 65/2$, which is below the maximum configuration spin of $I = 69/2$ at $\gamma = 60^\circ$.

For the bands 6, 7, 8, and 9 the lack of experimental information prevents an unambiguous assignment of configurations.

Summarizing the results for the positive-parity states, any evidence for an oblate deformation at high spin could not be found. In the ground-state band the presumably prolate deformation at low spins stays up to the maximum configuration spin slightly tending to noncollective triaxiality. In contrast, band 5 is predicted to terminate at $I = 65/2$.

The yrast states of negative-parity form band 2 in the low-spin region. Spin and parity of the band head as well

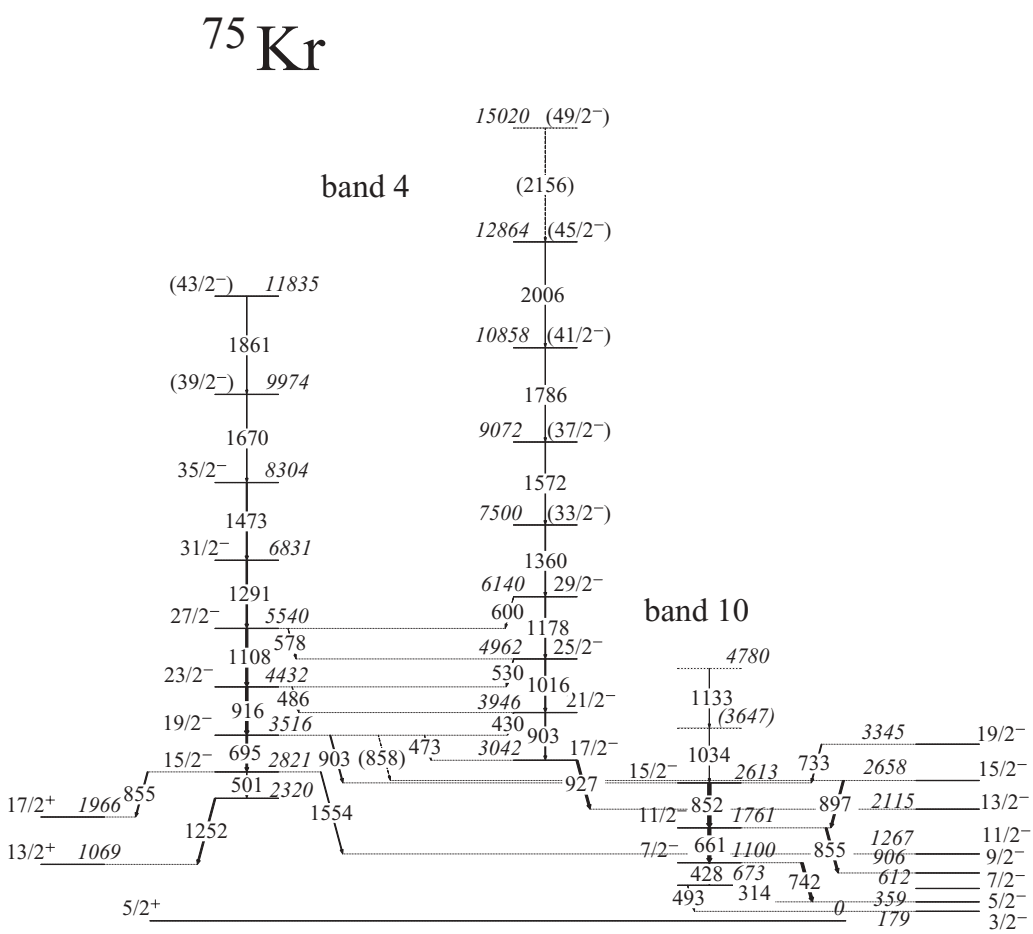

FIG. 11. Negative-parity states building band 4 and 10 are shown. On the right, the linking transitions to other excited levels in ^{75}Kr are drawn.

as the ones of the low-lying excited states are well established. The deexcitation pattern, indicating the nucleus to be in the strong coupling limit, suggests $K > 1/2$. In combination with the $I^{\pi} = 3/2^{-}$ band head and the low excitation energy the only solution is a configuration with the unpaired neutron in the [301]3/2 orbit (see Fig. 1). Starting from the energy gaps at prolate and oblate deformation, respectively, this would most probably be equivalent to a configuration with two protons and four neutrons in the $g_{9/2}$ orbit. In the oblate case a configuration including two protons and two neutrons in the $g_{9/2}$ orbit would also be possible. Assuming prolate deformation, this should lead to a reduced deformation in the low spin-region in comparison to band 1. The irregular decay pattern in the positive-signature branch of band 3 indicates a crossing at approximately $\hbar\omega = 0.4$ MeV. This may be explained with a transition from a 3qp configuration at higher spin to a 1qp configuration beneath the crossing. As in band 5, such a 3qp configuration should consist of the unpaired neutron and a broken fp-shell proton pair which is preferred due to Coriolis effects. The proton breakup leading most likely to three protons in the $g_{9/2}$ orbit would also explain the absence of another strong up- or back-bending in band 3 above $\hbar\omega \approx 0.4$ MeV. In agreement with these considerations, the CNS calculations predict a (2,4) configuration to be the lowest in energy for both positive- and negative-signature states (see Fig. 14). These configurations reproduce the slope of the excitation-energy curves with rising spin qualitatively and are therefore assigned to band 2.

Band 3 shows an inverse signature splitting favoring the negative-signature states. Assuming a closed ^{56}Ni core, this signature splitting and also the development of the excitation energies with spin are very well reproduced by the (3,5)-1 configuration.

Even the excitation energies relative to the (2,4) configuration are comparable to the ones experimentally observed, taking the systematic underestimate of the excitation energies of the two-proton configurations into account. For comparison only, the drawn energies of the configuration (2,4) were shifted up by 0.6 MeV [labels $(2,4)_s$ in Fig. 14]. Allowing a breaking ^{56}Ni core, the situation seems to be more complicated. In this case, there are two additional signature partners occurring, which are favored in the low- and mid-spin region in comparison to the (3,5)-1 configuration (cf. Fig. 14). In contrast to the (3,5)-1 configurations, they do not reproduce the experimental signature splitting at all.

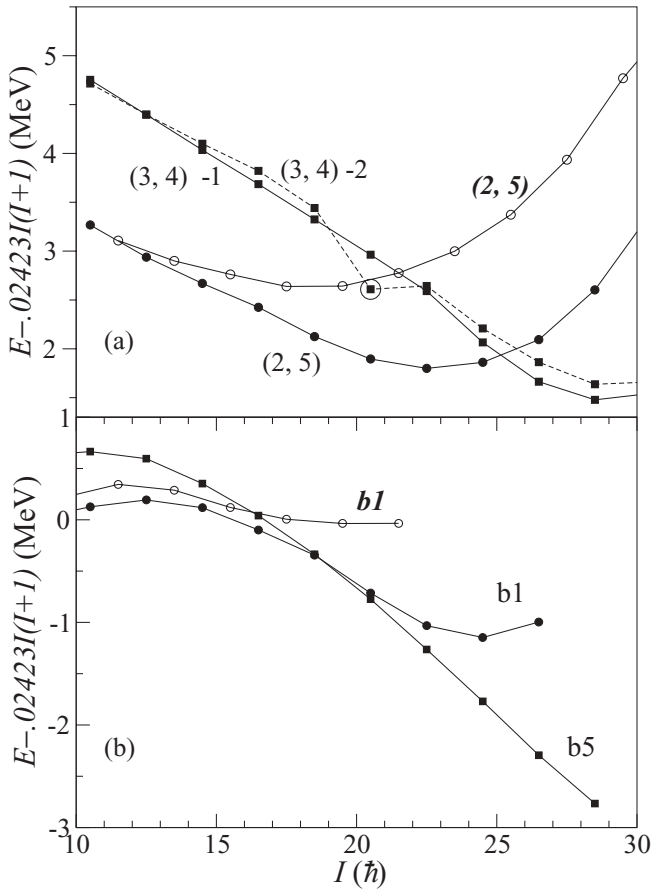

FIG. 12. Experimental (bottom) and calculated excitation energies (top), corrected for the contribution of a rigid rotor for the positive-parity states in ^{75}Kr. The positive- and negative-signature level energies are marked with filled and open symbols, respectively. The experimental bands are labeled b. The calculated energies of the energetically favored configurations reproduce the experimental level energies well. The overstimate of energies calculated for band 5 with respect to band 1, which systematically occurs for configurations with more than two particles in the $g_{9/2}$ orbits, is the consequence of too high single-particle energies of the $g_{9/2}$ orbits. The large open circles in this figure mark the calculated energies, for which the minimum in the potential energy surfaces is located at $\gamma = 60^\circ$ or $\gamma = -120^\circ$.

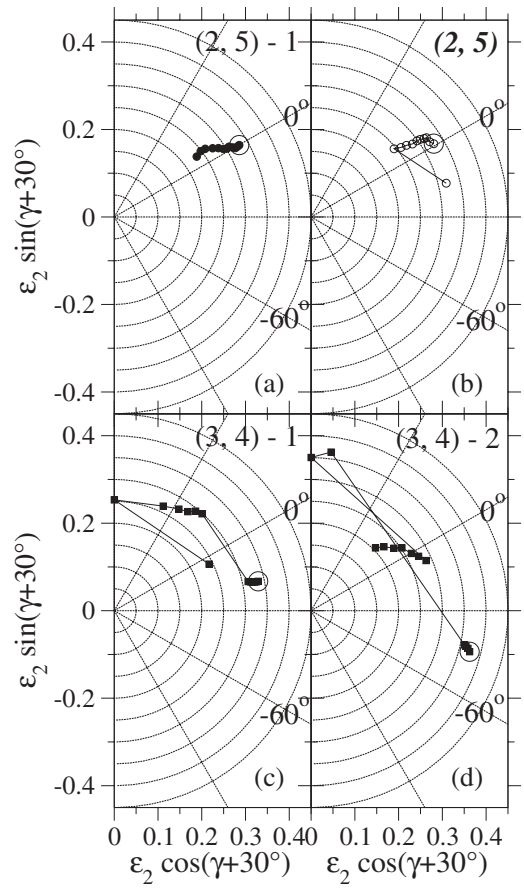

FIG. 13. Deformation paths formed by the positions of minimum energy in the potential energy surfaces in the ϵ_2-γ plane for the different spin values. The paths are shown for the configurations assigned to the positive-parity bands 1 and 5. The large open circles in this type of figure always mark the minimum in the ϵ_2-γ plane belonging to the lowest calculated spin (see Fig. 12). Here and in the following, the deformation parameters are used in the Lund convention.

Hence, the association of the (2,4) and the (3,5)-1 configurations at a closed ^{56}Ni-core with bands 2 and 3, respectively, is considered unambiguous. The unusual band crossing observed in band 3 at $\hbar\omega \approx 0.4$ MeV may therefore represent the transition from the nearly prolate 3qp to the tentative mainly oblate 1qp state.

The deformations in the negative- and positive-signature branches are close to the ones at the calculated initial spins of $I = 21/2$ and $I = 23/2$, respectively, located in the proximity of $\gamma = 0$ (see Fig. 15). In contrast to band 2, where a trend to less collectivity and a reduction of the deformation to $\epsilon_2 \approx 0.2$ with rising spin is found, the deformation in band 3 stays at collective values of $\epsilon_2 > 0.25$ up to the maximum configuration spin.

For band 4, the situation is comparably unambiguous as may be seen in Fig. 14 (top). In this case the two possible candidates (3,5)-2 and (3,5)-3 were found to reproduce the signature splitting and the development of the excitation energies with rising spin qualitatively. They are presented in the figure by triangles: open for negative and filled for positive signature. For further predicted energetically favored configurations either the development of the excitation energies or the small signature splitting is not described.

Taking the single-particle energy dependence into account by applying a globally adjusted parameter set, not only the assignments to bands 2 and 3 are supported, but also the association of band 4 with the (3,5)-3 configuration is favored. This is a consequence of the shift up in energy for the configurations containing a broken ^{56}Ni core as, e.g., (3,5)-2 and (3,5)-3 in the global parameter set.

As in band 3 the deformation of the nucleus stays close to collective prolate up to the maximum spin of this configuration. Merely for the states of highest spins it is slightly tending to collective triaxiality with $\gamma \approx 10^\circ$ (see Fig. 15). Due to the polarizing effect of the hole in the $f_{5/2}$ shell, the initial quadrupole deformation $\epsilon_2 \approx 0.37$ at spin $I \approx 10$ is larger

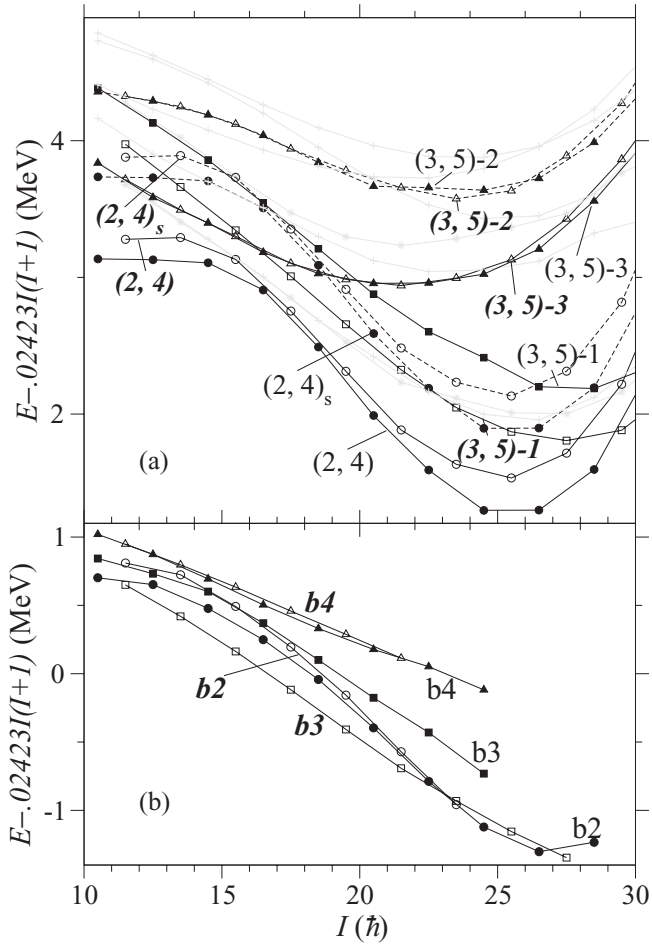

FIG. 14. Experimental (bottom) and calculated excitation energies (top) of the negative-parity bands in ^{75}Kr, corrected for the contribution of a rigid rotor. The positive- and negative-signature level energies of the assigned configurations are marked with filled and open symbols, respectively. Other configurations, predicted to lie low in energy, are labeled with plus and star symbols. The experimental energies of the bands are labeled with the abbreviation "b". An "s" has been appended to the label of those configurations that were corrected for systematic energetical underestimates by adding 0.6 MeV (see text for details).

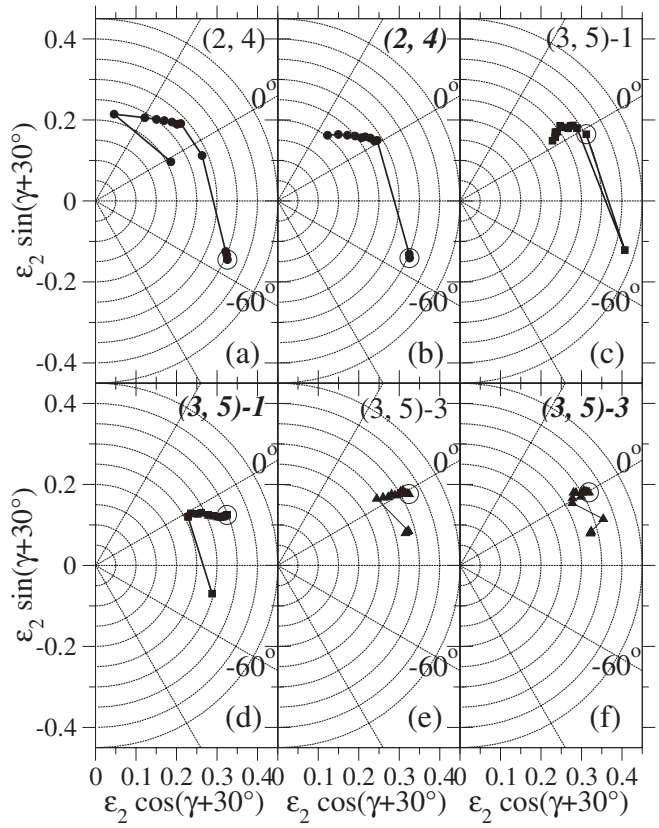

FIG. 15. Deformation paths consisting of the positions of the energy minima in the potential energy surfaces for the different spins, shown for the configurations assigned to the negative-parity bands 2 and 3. The large open circles mark the minima in the ϵ_2-γ plane belonging to the lowest calculated spins (cf. Fig. 14).

compared to the configurations (2,4) and (3,5)-1. Within the band, it is predicted to decrease to $\epsilon_2 \approx 0.3$ close to the maximum configuration spin. As in the positive-parity states, also in the negative-parity bands any evidence for an oblate-prolate shape coexistence at high spins has not been found, as it has been identified in ^{76}Rb, lately [39]. In ^{76}Rb coexisting oblate and prolate shapes were found up to spin $I = 31$.

VII. CONCLUSION

In conclusion, the level scheme of ^{75}Kr has been considerably extended in the present work. This includes the revision of the level scheme proposed by in earlier work as well as more than 100 newly identified or placed transitions and about 70 levels established for the first time. Furthermore, the performed DCO analysis supported the former spin assignments in most cases and yielded about 60 new spin assignments. The newly identified or extended high-spin bands in ^{75}Kr are described well within the CNS approximation. The results thereby not only match the expectations for the low-spin region derived from a simplified model as the single-particle energies in a deformed potential, but also fit systematically well in the predictions of this approximation for the other neutron-deficient Kr isotopes.

It turns out that in spite of the shape coexistence at low spin no further indication for influences of an oblate deformation could be identified at high spin. Moreover, the nucleus is predicted to be mainly collective prolate deformed, slightly tending to noncollective triaxiality in the bands 1, 2, and 4 close to the maximum configuration spin.

ACKNOWLEDGMENTS

The authors wish to thank Ingemar Ragnarsson for the introduction in the configuration-dependent cranked Nilsson-Strutinsky approach and the guidance while performing the calculations. This work was supported by the German BMBF under Contract No. 06K167.

[1] S. L. Tabor, Phys. Rev. C **34**, 311 (1986).
[2] M. Wiosna, J. Busch, J. Eberth, M. Liebchen, T. Mylaeus, N. Schmal, R. Sefzig, S. Skoda, and W. Teichert, Phys. Lett. B **200**, 255 (1988).
[3] C. J. Lister, B. J. Varley, H. G. Price, and J. W. Olness, Phys. Rev. Lett. **49**, 308 (1982).
[4] I. Stefanescu, J. Eberth, G. de Angelis, N. Warr, G. Gersch, T. Steinhardt, O. Thelen, D. Weisshaar, T. Martinez, A. Jungclaus *et al.*, Phys. Rev. C **69**, 034333 (2004).
[5] W. Nazarewicz, J. Dudek, R. Bengtsson, T. Bengtsson, and I. Ragnarsson, Nucl. Phys. A **435**, 397 (1985).
[6] E. Bouchez, I. Matea, W. Korten, F. Becker, B. Blank, C. Borcea, A. Buta, A. Emsallem, G. de France, J. Genevey *et al.*, Phys. Rev. Lett. **90**, 082502 (2003).
[7] S. M. Fischer, C. J. Lister, D. P. Balamuth, R. Bauer, J. A. Becker, L. A. Bernstein, M. P. Carpenter, J. Durell, N. Fotiades, S. J. Freeman *et al.*, Phys. Rev. Lett. **87**, 132501 (2001).
[8] G. de Angelis, C. Fahlander, A. Gadea, E. Farnea, W. Gelletly, A. Aprahamian, D. Bazzacco, F. Becker, P. G. Bizzeti, A. Bizzeti-Sona *et al.*, Phys. Lett. B **415**, 217 (1997).
[9] N. S. Kelsall, R. Wadsworth, A. N. Wilson, P. Fallon, A. O. Macchiavelli, R. M. Clark, D. G. Sarantites, D. Seweryniak, C. E. Svensson, S. M. Vincent *et al.*, Phys. Rev. C **64**, 024309 (2001).
[10] F. Becker, W. Korten, F. Hannachi, P. Paris, N. Buforn, C. Chandler, M. Houry, H. Hubel, A. Jansen, Y. L. Coz *et al.*, Eur. Phys. J. A **4**, 103 (1999).
[11] C. Chandler, P. H. Regan, C. J. Pearson, B. Blank, A. M. Bruce, W. N. Catford, N. Curtis, S. Czajkowski, W. Gelletly, R. Grzywacz *et al.*, Phys. Rev. C **56**, R2924 (1997).
[12] C. Chandler, P. H. Regan, B. Blank, C. J. Pearson, A. M. Bruce, W. N. Catford, N. Curtis, S. Czajkowski, P. Dessagne, A. Fleury *et al.*, Phys. Rev. C **61**, 044309 (2000).
[13] C. J. Gross, J. Heese, K. P. Lieb, L. Luhmann, B. Wormann, A. A. Chishti, W. Gelletly, C. J. Lister, J. H. McNeill, and B. J. Varley, Z. Phys. A **331**, 361 (1988).
[14] C. J. Gross, J. Heese, K. P. Lieb, S. Ulbig, W. Nazarewicz, C. J. Lister, B. J. Varley, J. Billowes, A. A. Chishti, J. H. McNeill *et al.*, Nucl. Phys. A **501**, 367 (1989).
[15] S. Skoda, Ph.D. thesis, Universität zu Köln, 1992.
[16] S. Skoda, F. Becker, T. Burkardt, J. Eberth, S. Freund, U. Hermkens, T. Mylaeus, R. Sefzig, W. Teichert, A. von der Werth *et al.*, Nucl. Phys. A **633**, 565 (1998).
[17] N. G. Nicolis and J. R. Beene, program EVAPOR, 1993 (unpublished).
[18] F. Pühlhofer, Nucl. Phys. A **280**, 267 (1977).
[19] F. A. Beck, Prog. Part. Nucl. Phys. **28**, 443 (1992).
[20] E. Farnea, G. de Angelis, M. D. Poli, D. D. Acuna, A. Gadea, D. R. Napoli, P. Spolaore, A. Buscemi, R. Zanon, R. Isocrate *et al.*, Nucl. Instrum. Methods Phys. Res., Sect. A **400**, 87 (1997).
[21] O. Skeppstedt, H. A. Roth, L. Lindstrom, R. Wadsworth, I. Hibbert, N. Kelsall, D. Jenkins, H. Grawe, M. Gorska, M. Moszynski *et al.*, Nucl. Instrum. Methods Phys. Res., Sect. A **421**, 531 (1999).
[22] O. Stuch, Ph.D. Thesis, Universität zu Köln, 1997 (unpublished).
[23] D. C. Radford, Nucl. Instrum. Methods Phys. Res., Sect. A **361**, 306 (1995).
[24] J. Theuerkauf, S. Esser, S. Krink, M. Luig, N. Nicolay, O. Stuch, and H. Wolters, program TV, Universität zu Köln, Germany, 1992 (unpublished).
[25] R. M. Steffen and K. Alder, in *The Electromagnetic Interaction in Nuclear Spectroscopy*, edited by W. D. Hamilton (North-Holland, Amsterdam, 1975).
[26] M. K. Kabadiyski, K. P. Lieb, and D. Rudolph, Nucl. Phys. A **563**, 301 (1993).
[27] G. Winter, J. Döring, W. D. Fromm, L. Funke, P. Kemnitz, and E. Will, Z. Phys. A **309**, 243 (1983).
[28] G. Garcia Bermudez, C. Baktash, and C. J. Lister, Phys. Rev. C **30**, 1208 (1984).
[29] M. A. Herath-Banda, A. V. Ramayya, L. Cleemann, J. Eberth, J. Roth, T. Heck, N. Schmal, T. Mylaeus, W. Koenig, B. Martin *et al.*, J. Phys. G **13**, 43 (1987).
[30] A. A. Chishti, W. Gelletly, C. J. Lister, J. H. McNeill, B. J. Varley, D. J. G. Love, and O. Skeppstedt, Nucl. Phys. A **501**, 568 (1989).
[31] D. F. Winchell, M. S. Kaplan, J. X. Saladin, H. Takai, J. J. Kolata, and J. Dudek, Phys. Rev. C **40**, 2672 (1989).
[32] M. A. Cardona, G. Garcia Bermudez, A. Filevich, and E. Achterberg, Phys. Rev. C **42**, 591 (1990).
[33] S. Skoda, J. L. Wood, J. Eberth, J. Busch, M. Liebchen, T. Mylaeus, N. Schmal, R. Sefzig, W. Teichert, and M. Wiosna, Z. Phys. A **336**, 391 (1990).
[34] T. Trivedi, R. Palit, D. Negi, Z. Naik, Y.-C. Yang, Y. Sun, J. A. Sheikh, A. Dhal, M. K. Raju, S. Appannababu *et al.*, Phys. Rev. C **80**, 047302 (2009).
[35] Y.-C. Yang, Y. Sun, T.Trivedi, R. Palit, and J. A. Sheikh, Int. J. Mod. Phys. E **19**, 1754 (2010).
[36] M. Keim, E. Arnold, W. Borchers, U. Georg, A. Klein, R. Neugart, L. Vermeeren, R. E. Silverans, and P. Lievens, Nucl. Phys. A **586**, 219 (1995).
[37] A. V. Afanasjev, D. B. Fossan, G. J. Lane, and I. Ragnarsson, Phys. Rep. **322**, 1 (1999).
[38] L. Grodzins, Phys. Lett. **2**, 88 (1962).
[39] R. Wadsworth, I. Ragnarsson, B. G. Carlsson, H.-L. Ma, P. J. Davies, C. Andreoiu, R. A. E. Austin, M. P. Carpenter, D. Dashdorj, S. J. Freeman *et al.*, Phys. Lett. B **701**, 306 (2011).